

Microstructure, Hardness, Tensile Strength, and Sliding Wear of Hypoeutectic Al–Si Cast Alloys with Small Cr Additions and Fe-Impurity Content

Eduardo de Rosso, Carlos A. dos Santos,* and Amauri Garcia

Herein, the influence of Cr additions on the solidification parameters, as-cast microstructures, and mechanical properties of Al–Si alloys with Fe-impurity is investigated. Al–Si–Cr alloys with 3% and 7% Si and 0.25% and 0.40% Cr are developed. Solidification experiments are performed using an instrumented cooling casting apparatus permitting the obtainment of vertical upward-solidified ingots. The morphological and phase structures are characterized by optical and scanning electron microscopy and X-ray diffractometry. Hardness, tensile, and dry sliding wear tests are conducted to determine the mechanical properties. The Cr addition to the Al–Si alloys leads to the formation of α -Al(Si, Fe)Cr interdendritic precipitates, suppressing the formation of undesired needle-like β -intermetallic compounds (Al_5FeSi). It is noted that both higher alloy Cr content and cooling rate induce refinement in the dendrite arm spacing, and improvement in both hardness and ultimate tensile strength when considering the alloys with identical Si content. The coefficient of friction slightly increases with increasing alloy Cr content and with coarsening of the microstructure. Correlations between the wear rate and secondary dendrite arm spacing are proposed, in which the wear rate decreases with decrease in the secondary dendrite arm spacing and increase in the alloy Cr content and hardness.

and aerospace applications.^[2–6] The as-cast microstructure of Al–Si hypoeutectic alloys generally shows a dendritic structure with isolated Si and impurities as secondary phases in the interdendritic regions. The most deleterious feature related to Al–Si cast alloys is the presence of Fe that frequently appears as an impurity in conventional casting processes. Due to the low solid solubility in the α -Al matrix, Fe is segregated into the liquid during solidification and forms intermetallic compounds. Several works have shown that the presence of Fe in Al–Si cast alloys negatively changes the mechanical properties associated with the ductility due to the needle-like morphology and brittleness of the β - Al_5FeSi (β -phase, monoclinic).^[7–11] The β -phase formation depends not only on the Fe content but also on the cooling rate conditions during solidification evolution, as reported in some works.^[12–14] In general, the amount of β -phase increases, whereas the solidification rate decreases, mainly in those ranges observed in conventional casting processes. To solve the problem,

1. Introduction

The extensive application of Al–Si alloys in the foundry industry is due to their enhanced metallurgical aspects such as excellent castability, improved mechanical properties, recyclability, and high strength-to-weight ratio when compared with cast-iron alloys.^[1] Despite these advantages, modern industry requires alloys with enlarged responses related to high tribology and corrosion resistances, especially for automotive, aeronautical,

additions of transition metals, such as Mn, Cr, Zr, Ni, Be, V, Co, and Ti, are used to change the morphology of the β -particles. Among these elements, Mn is often used for this purpose due to its effectiveness. According to Shabestari and collaborators,^[15,16] small additions of Mn can avoid the β -phase formation, inducing the formation of other less harmful intermetallics. Cao and Campbell^[17] and Bidmeshki et al.^[18] have confirmed that a Mg:Fe ratio up to 0.5 changes the morphology of the β -particles from needle-like to star-like polygonal in Al–Si alloys.

Similarly, the effects of Cr and mixtures with other elements on the microstructure and mechanical properties have been evaluated by several authors. As the atomic radius, crystal structure, and atomic number of Cr and Mn are close, it might be expected that Cr would have an efficient behavior to modify and/or eliminate the β -phase.^[19] Li et al.^[20] verified the formation of α -Al(Fe, Cr)Si phases after addition of 0.5% Cr to an Al–Si piston alloy with 0.8% Fe. Yang et al.^[21] investigated the effect of different Cr additions to the microstructure and mechanical properties of a eutectic Al–Si alloy and demonstrated that the conversion from β - Al_5FeSi to α -Al(Fe, Cr)Si improved mechanical responses, especially in terms of ductility. A work reported by Grushko and Pavlyuchkov^[22] observed identical positive variation

E. de Rosso, Prof. C. A. dos Santos

School of Technology

Pontifícia Universidade Católica do Rio Grande do Sul – PUCRS

Av. Ipiranga, 6681, 90.619-900 Porto Alegre, RS, Brazil


E-mail: carlos.santos@pucrs.br

Prof. A. Garcia

Department of Manufacturing and Materials Engineering

University of Campinas – UNICAMP,

13 083-860 Campinas, SP, Brazil

 The ORCID identification number(s) for the author(s) of this article can be found under <https://doi.org/10.1002/adem.202001552>.

DOI: 10.1002/adem.202001552

in mechanical properties. Cui et al.^[23] also proposed an approach to eliminate the formation of the β -Al₅FeSi intermetallic compound by adding Cr to Al–Si alloys, inducing the precipitation of α -Al(Fe, Cr)Si phases. Moreover, aspects such as grain size and morphology, microstructure features, and the presence of intermetallic particles are used to correlate the positive effect of Cr on mechanical properties, wear, and corrosion behavior.^[5,24,25] Although there are studies focusing on the metallurgical and mechanical characteristics of Al-based alloys with Cr additions, the lack of information on as-cast Al–Si alloys with

different Si:Cr ratios and the correlation with solidification conditions and microstructure formation have motivated the current study. The aim of this work is to investigate the effects of Cr additions (0.25 and 0.4 wt%) on the solidification parameters (tip growth rate, liquid thermal gradient, and cooling rate), microstructure features (macrostructure and microstructure), and mechanical properties (hardness, tensile, and dry-wear responses) of two as-cast Al–3%Si and Al–7%Si alloys containing Fe as impurity.

2. Experimental Section

2.1. Material Preparation

The Al–12Si (wt%) master alloy ingot and additions of pure aluminum (>99.8% purity) and chromium (>99.7% purity) were used to prepare four alloys with compositions of Al–3Si–0.25Cr, Al–3Si–0.40Cr, Al–7Si–0.25Cr, and Al–7Si–0.40Cr, which were melted using a heat resistance pit furnace. Silicon carbide crucibles covered with boron nitride were used to obtain \approx 4 kg of each alloy. After melting of the master alloy, pure Al and Cr in the form of small blocks were

Table 1. Identifications and chemical composition of the 332, 334, 372, and 374 alloys (wt%).

Alloy	Si	Cr	Fe	Cu	Mn	[Mg]	Ni	Zn	Al
332	3.01	0.23	0.440	0.031	0.020	0.005	0.034	0.033	Balance
334	2.91	0.46	0.459	0.005	0.009	0.006	0.050	0.001	Balance
372	7.58	0.26	0.229	0.006	0.002	0.001	0.010	0.001	Balance
374	6.88	0.46	0.454	0.021	0.007	0.002	0.045	0.002	Balance

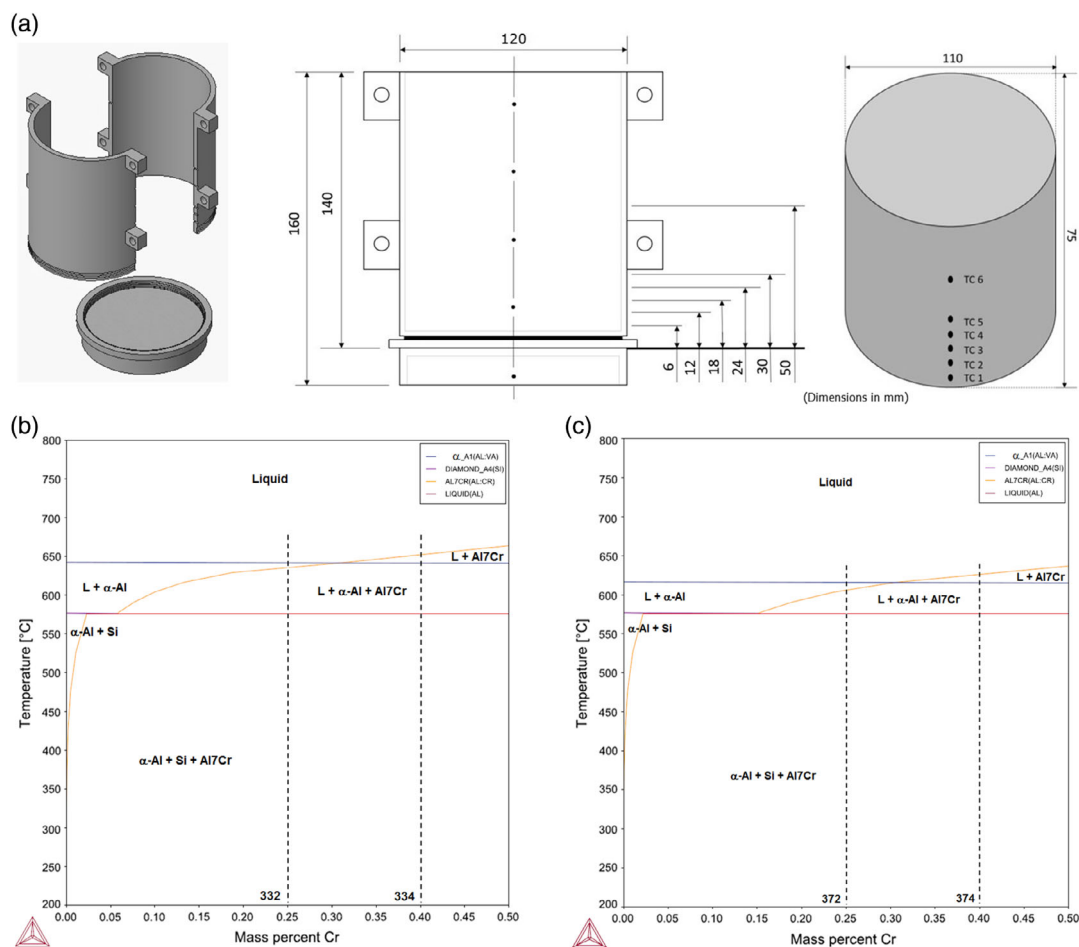


Figure 1. a) Representation of the metallic mold and alloy ingot, b) Al–3Si–xCr, and c) Al–7Si–xCr partial pseudobinary equilibrium phase diagrams (dashed vertical lines: nominal Cr contents).

added to the melt at 850 °C. Grain refiner elements were not used so as to preserve the as-cast microstructure unmodified. The melt was held for 3 h under mechanical stirring at intervals of 15 min to ensure the complete dissolution of Cr. After that, the melt was cooled down to 740 °C and then poured into open cast-iron molds. Samples extracted from the solidified ingots were subjected to spark emission spectrometry (Spectro, SpectroMaxx) to certify the chemical compositions. Five measurements in each alloy, hereinafter referred to as 332 (3Si–0.25Cr), 334 (3Si–0.40Cr), 372 (7Si–0.25Cr), and 374 (7Si–0.40Cr) alloys, were taken, resulting in the average values shown in **Table 1**. All alloys exhibited chemical compositions closer to the nominal composition in relation to Si and Cr contents. The Fe content is probably due to the contamination from the contact between the molten metal and accessories used during melting and its presence in the raw materials.

A vertical upward solidification apparatus consisting of a tubular furnace with two resistive heating zones and a bipartitioned cylindrical SAE 1020 steel mold (**Figure 1a**) cooled at the bottom with a water flow rate of $4 \pm 0.1 \text{ L min}^{-1}$ was used to remelt the alloys. Further details about the solidification apparatus are given in previous studies.^[26,27] In the experiments, the cooling system was started when the molten metal temperature reached the superheat above 10% of each alloy's *liquidus* temperature. Six K-type thermocouples with 1.6 mm diameter were positioned inside the mold with a view to obtaining the thermal evolution profiles during solidification with an acquisition rate of 10 Hz. The experiments permitted solidifying of two identical ingots in height, diameter, and weight (about 2 kg) for each alloy. The liquidus temperatures were determined based on the partial Al–3Si–xCr and Al–7Si–xCr pseudobinary equilibrium phase diagrams simulated by the Thermo-Calc software, as shown in **Figure 1b,c**.

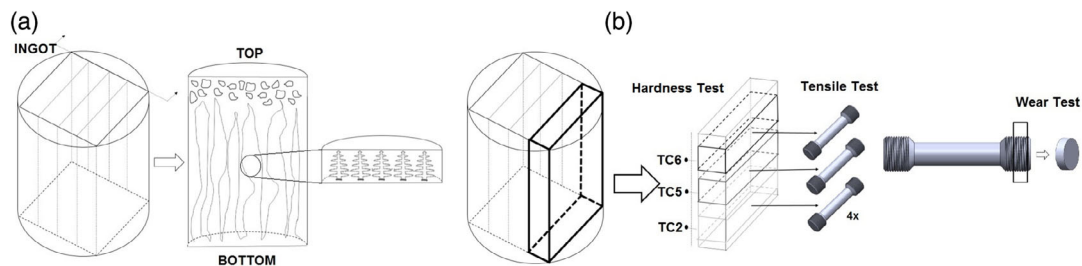


Figure 2. a) Representation of the solidified ingot and b) samples/specimens extracted for mechanical testing.

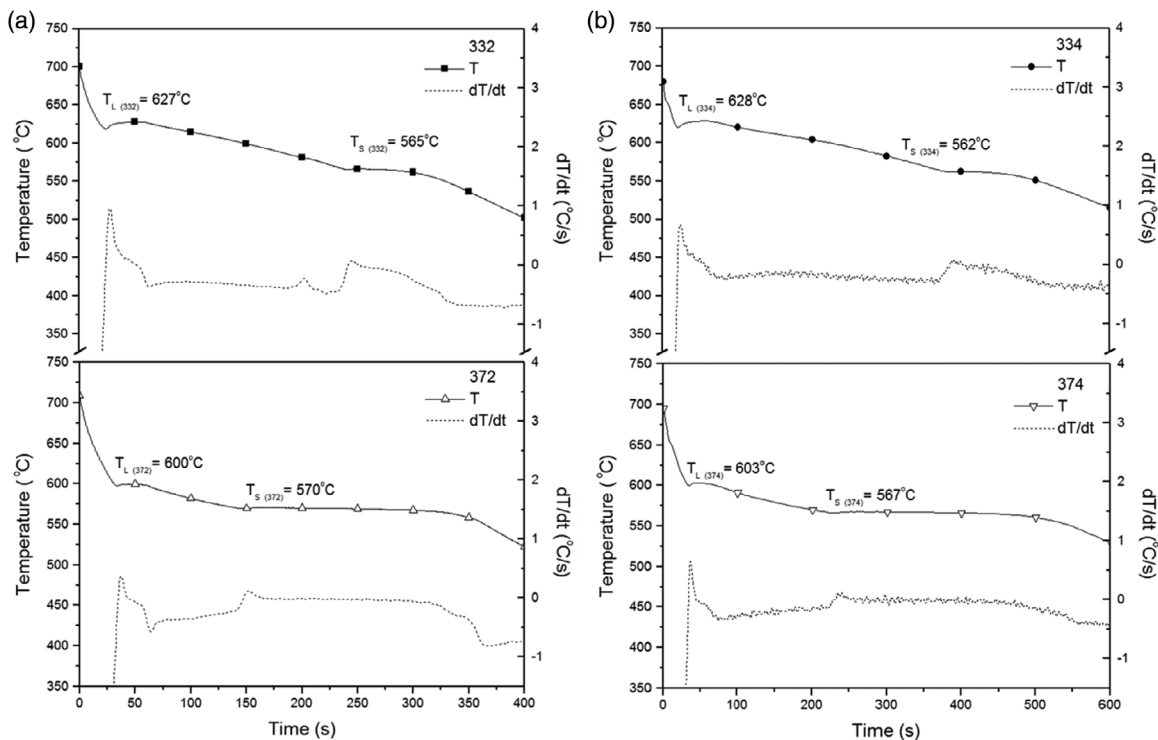


Figure 3. Cooling and first derivative curves of the a) 332 and 372 and b) 334 and 374 alloys.

2.2. Microstructure and Mechanical Tests

Samples for metallography analyses were extracted from the longitudinal and transversal sections of the ingots as shown in **Figure 2a** and prepared by grinding, polishing, and etching according to standard metallographic techniques.^[28,29] For revealing the macrostructure, modified Keller's reagent (10 mL HF, 60 mL HCl, 20 mL HNO₃, and 270 mL distilled water) was used and fluoride acid (5% HF in distilled water) for microstructure observation by optical microscopy (Olympus, PMG). For scanning electron microscopy (FEI, Inspect F50) and energy-dispersive X-ray spectroscopy (Oxford), electrolytic polishing and etching was utilized (Buehler, Electromet 4). The X-ray diffraction analyses (Shimadzu, XRD -7000, Cu K α 1 radiation, 40 kV, 30 mA, 2 θ : 10°–100°) were performed using powders obtained from each alloy ingot by a machining process.

Brinell hardness tests (PWE, 5 mm WC ball indenter, 2500 N load, 30 s dwell time), as recommended by the ASTM E10 standard test method,^[30] were conducted at specific positions from the cooled bottom (12; 30 and 50 mm distance from the bottom of the ingot, corresponding to the TC2, TC5, and TC6 thermo-couple locations). Tensile test specimens were extracted from the ingots as shown in **Figure 2b**, prepared according to the ASTM Standard E8/E8M-16a,^[31] and tested using a universal testing machine (Shimadzu, 30 kN). Four specimens were taken from each location and the average values were determined.

Microhardness Vickers measurements (Shimadzu, HMV-G) were performed following the recommendations of the ASTM E92 standard method.^[32]

For dry sliding wear tests, 10 mm diameter/3 mm thick discs were cut from the grip section of the tensile specimens (**Figure 2b**). Before the tests, the discs were ground on both faces with sandpaper (#220, #320, #400, #600), cleaned, and air dried. A high frequency reciprocating rig (Ducom, 4.2) was used with a 5 N applied load, 1 mm stroke, 10 Hz, and 25 °C–60% humidity. SAE 52 100 chrome steel balls (6 mm diameter) were used as the counterface material due to their higher hardness (62-63 HRC) compared with those of the alloys, restricting surface damage of the pin. Wear tests were conducted in duplicate for each alloy and position (on both faces of the discs) and the average values of the coefficient of friction (COF) and wear rate (*W*) were determined.^[33,34]

3. Results and Discussion

3.1. Thermal Analyses and Solidification Conditions

Thermal analysis based on the computer-aided cooling curve analysis^[35] was adopted to confirm the liquidus (*T_L*) and solidus (*T_S*) temperatures for each alloy (**Figure 3a,b**). The molten alloy was poured into a cylindrical thermal analysis cup (30 mm height \times 50 mm internal diameter) with a K-type

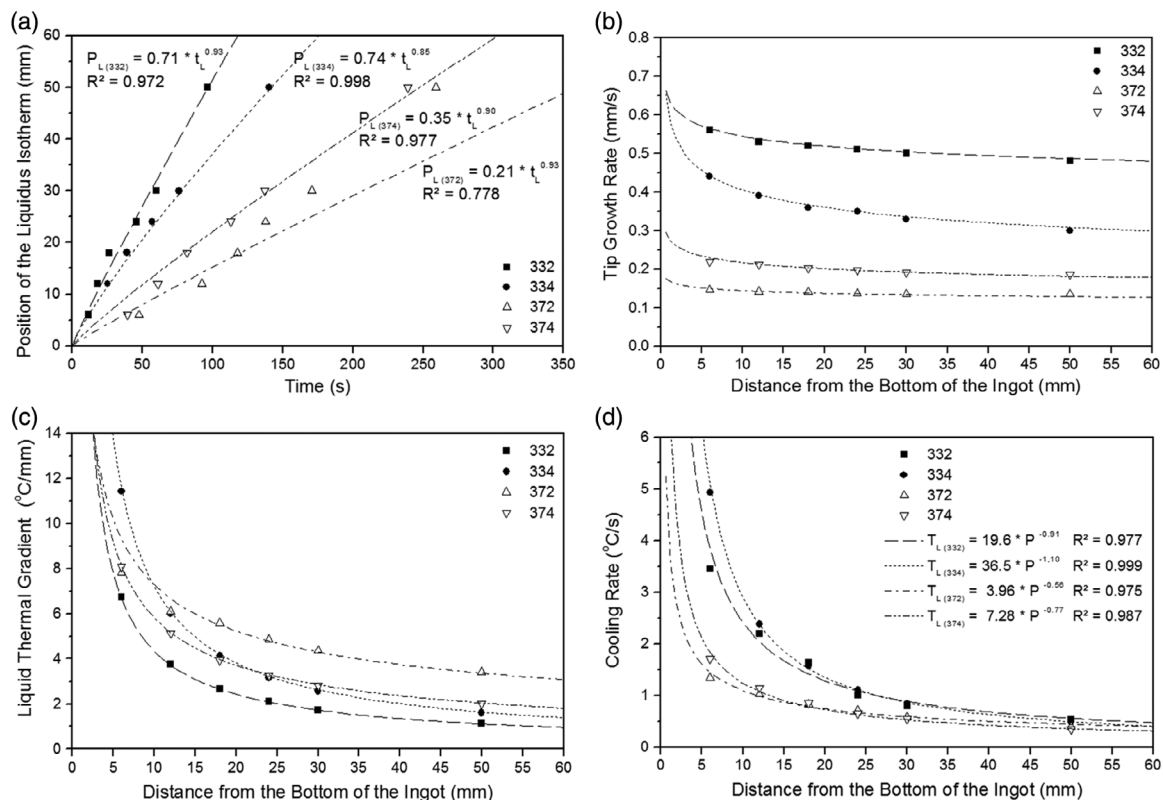


Figure 4. a) Liquidus isotherm, b) tip growth rate, c) liquid thermal gradient, and d) cooling rate variations as a function of position along the length of the solidified alloy ingots. R^2 is the coefficient of determination.

thermocouple located at the cup center. The first derivative curve obtained from the cooling curve was utilized to determine T_L and T_S .

For the 332 alloy (Al-3Si-0.25Cr), the liquidus temperature was determined at 627°C and the solidus temperature at 565°C, and the 334 alloy (Al-3Si-0.40Cr) had the experimental value of T_L at 628°C and that of T_S at 562°C. With the increase in

the alloy Si content, the 372 alloy (Al-7Si-0.25Cr) showed values of T_L at 600°C and T_S at 570°C and the 374 alloy (Al-7Si-0.40Cr) showed T_L at 603°C and T_S at 567°C. In all cooling curves, lower undercoolings were observed before the beginning of nucleation. The values of T_L are slightly greater than those observed in the equilibrium phase diagrams shown in Figure 1b,c both probably due to the presence of Fe as an impurity in the alloys. A similar

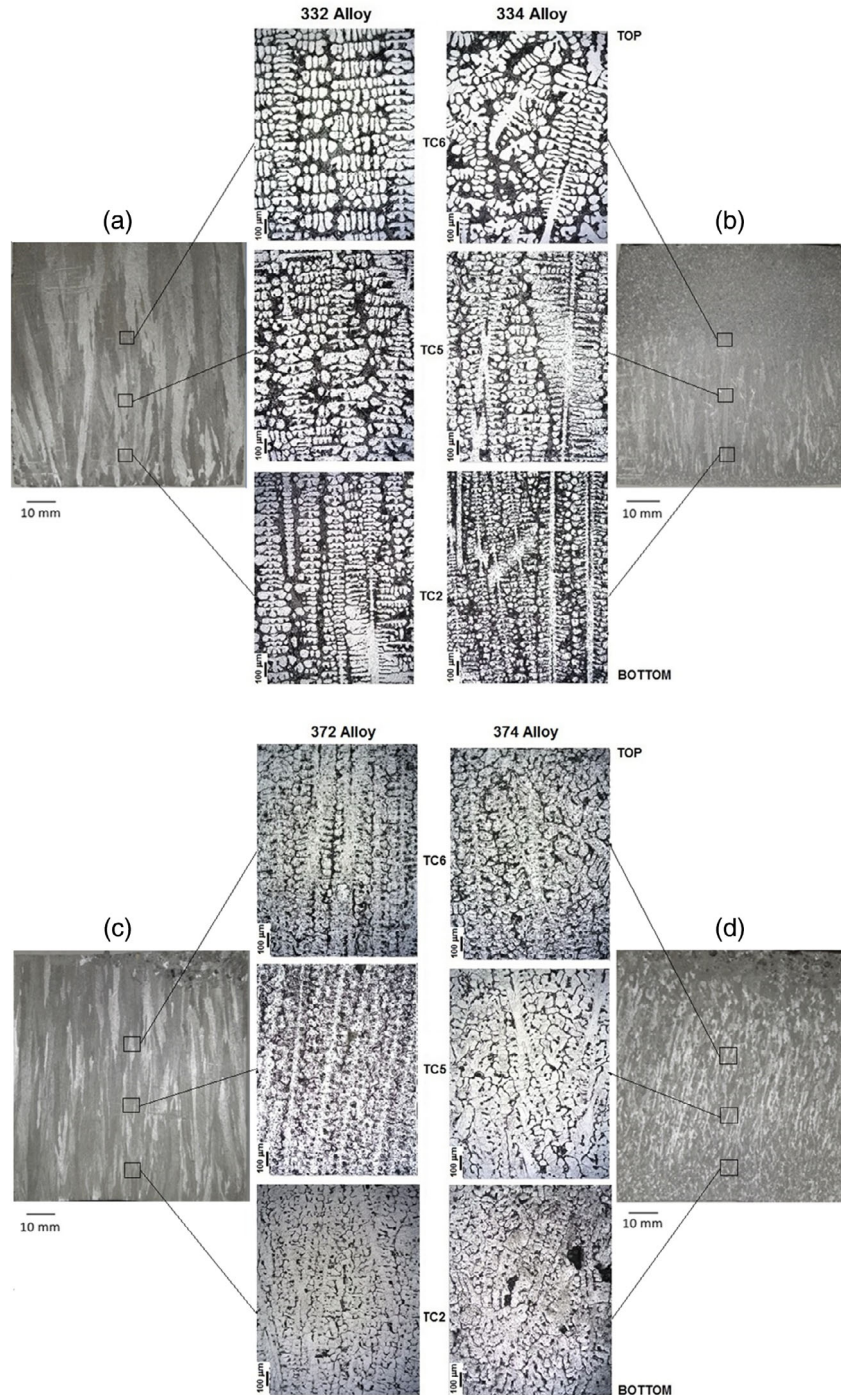


Figure 5. Longitudinal macrostructures and microstructures of the a) 332, b) 334, c) 372, and d) 374 alloys ingots.

observation was reported by Farahany et al.,^[36] who found a lower value of T_L after addition of 0.4% Fe to an Al–11% Si alloy when comparing to the T_L value of the binary Al–11% Si alloy without Fe.^[37]

After the directional solidification experiments, the acquired thermal profiles were used to obtain the position of the liquidus isotherm (T_L) as a function of time (t_L) for each thermocouple position along the length of the ingot, as shown in Figure 1a. The results are shown in Figure 4a, as well as the fitting equations that represent those evolutions. The solidification thermal parameters, such as the tip growth rate (V_L), liquid thermal gradient (G_L), and tip cooling rate (\dot{T}), were determined (Figure 4b,d), and experimental expressions as a function of position were also obtained for the cooling rates. The tip growth rate was obtained from the derivative of the function $P_L = f(t_L)$ with respect to time (t), and the cooling rate was calculated by deriving the temperature (T) with respect to time immediately after the passage of the liquidus isotherm by each thermocouple.

The tip growth rates for the alloys with lower Si content (332 and 334 alloys) showed higher values compared to those of the alloys with higher Si content (372 and 374 alloys), as shown in Figure 4b. It can be observed that the tip growth rates decreased with the increase in Cr addition for the alloys with lower Si content. In contrast, an increase in the alloys with higher Si content was noted. Regarding the liquid thermal gradient (Figure 4c), the alloys with 7% Si show higher values than those with 3% Si. An exception is observed for the 334 alloy, which is shown to have the highest liquid thermal gradient at positions near the cooled bottom of the ingot as a consequence of the highest liquid superheat before solidification. With Cr addition, the liquid thermal gradient decreases with the increase in the Cr content for the alloys with higher Si content and increases for the lower Si-containing alloys. An opposite behavior can be observed associated with the cooling rate (Figure 4d).

The alloys with lower Si content showed higher cooling rate values than the alloys with higher Si content, and the addition of Cr increased the cooling rates in the alloys when considering the same Si content. In the investigation reported by Peres et al.^[38] with binary Al–Si alloys containing 3, 5, 7, and 9% Si directionally solidified under unsteady–steady heat transfer conditions using a vertical upward solidification apparatus, the values of the tip growth rate and cooling rate as a function of alloy Si content were practically identical for all alloys. Similar behavior was also noted by Goulart et al.^[39] with two Al–Si alloys containing 5 and 9% Si solidified in a horizontal solidification apparatus. The observed difference between the present results and those related in the literature indicates that the Cr addition significantly influences the solidification thermal parameters.

3.2. Microstructural Analyses

Figure 5 shows the morphology of the longitudinal macrostructures. All the solidified ingots exhibited columnar grains along the regions where the thermocouples were located. A difference between the 332 and 334 lower-Si-containing alloys (Figure 5a,b) can be noted. With 0.25% Cr addition, a complete columnar

macrostructure was obtained along the entire ingot, whereas a columnar-to-equiaxed transition is clearly observed for the 334 alloy with 0.40% Cr at ≈ 67 mm from the cooled bottom of the ingot. The columnar-to-equiaxed transition probably occurs due to the higher G_L values compared to the 332 alloy, as shown in Figure 4c. In the case of the alloys with higher Si content, the 372 alloy with 0.25% Cr showed a predominant columnar macrostructure (Figure 5c) with a small equiaxed region close to the top of the ingot (≈ 90 mm), whereas the increase in the Cr addition of the 374 alloy induced a columnar-to-equiaxed transition at ≈ 80 mm from the metal/mold interface (Figure 5 d). As reported by Peres et al.^[38] referring to Al–Si alloys, columnar structures prevail when the solidification cooling rate is greater than $0.2\text{ }^\circ\text{C s}^{-1}$. In the investigation herein, the columnar-to-equiaxed transition of the examined Al–Si–Cr alloys was shown to occur at $\approx 0.25\text{ }^\circ\text{C s}^{-1}$. Analyzing the columnar region, it is possible to observe that the 334 and 374 alloys showed more refined grains compared to the 332 and 372 alloys. This can be attributed to the higher Cr content of the alloys. Cr is usually used as a grain refiner in Al-based alloys because Cr forms dispersed phases due to its lower diffusion rate into the Al-rich matrix, acting as a grain growth constrainer.^[40–42]

To correlate solidification conditions with a representative length scale of the microstructure, the secondary dendrite arm

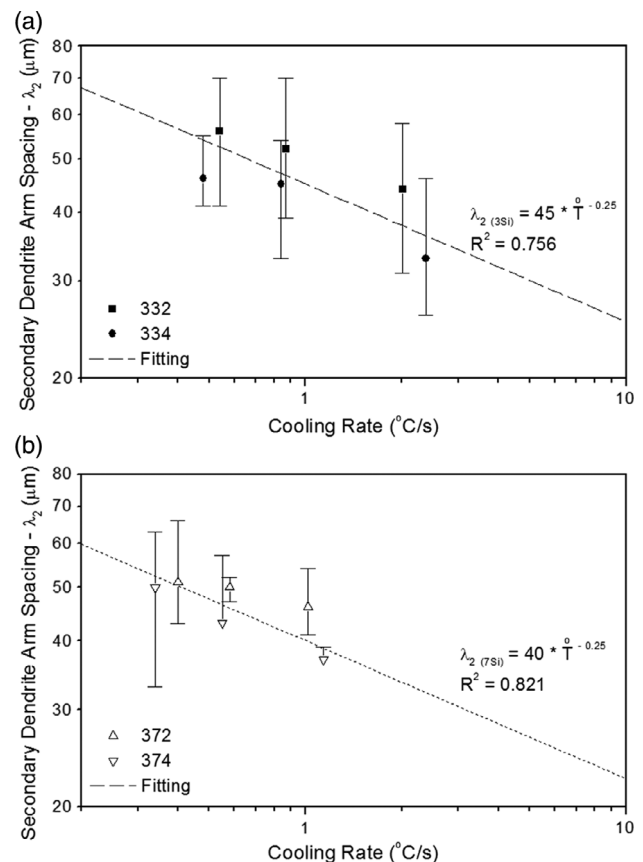


Figure 6. Evolution of secondary dendrite arm spacing (λ_2) with cooling rate (\dot{T}) along the length of the ingots: a) 332 and 372 and b) 334 and 374 alloys.

spacings (λ_2) were revealed for all the alloys. Figure 5 shows the microstructures at the positions corresponding to the TC2, TC5, and TC6 samples. For the 332 and 334 alloys with 3% Si, the unidirectional cooling effect clearly changes the morphology of the dendrites, causing a continuous increase in λ_2 from the bottom to the top of the ingots. For the 372 and 374 alloys with 7% Si the increase in λ_2 is not so evident because the dendrites have now a coarser aspect due to the lower cooling rates observed during solidification when compared to the alloys with 3% Si. Using the optical microscope, at least 20 measurements of λ_2 for each thermocouple position were performed. **Figure 6a,b** shows the evolution of λ_2 as a function of cooling rate (\dot{T}) for the positions 12, 30, and 50 mm from the metal/mold interface, showing that λ_2 increases with the decrease in \dot{T} . Experimental growth laws for λ_2 as a function of \dot{T} have been derived, and two power function equations with a single -0.25 exponent represent the variation of λ_2 for the alloys with different Si contents. Costa et al.^[43,44] found a similar equation for ternary Al–Cu–Si alloys, however with a -0.33 exponent representing the variation in $\lambda_2 = f(\dot{T})$. According to Zang et al.,^[45] the Si content has a significant effect on the size of λ_2 at higher cooling rates and Djurdjevic and Grzincic^[46] have attributed this behavior to the solute redistribution during solidification.

Figure 7 and **8** show SEM images of the alloy microstructures and details of the phases for the position at 12 mm from the bottom of the ingots, corresponding to the thermocouple TC2. The microstructure of all alloys is composed of a dendritic α -Al matrix (gray areas) with secondary phases in the interdendritic regions (white areas). The energy dispersive spectroscopy (EDS) analyses confirmed the presence of both Si particles in the eutectic mixture and the α -Al(Fe,Si)Cr intermetallic phase in the interdendritic zones with a “Chinese script” morphology, which is in agreement with Gustafsson et al.^[7] Zhan and Hu^[47] reported that this intermetallic replaces the needle-like β -Al₃FeSi phase due to the addition of Cr, confirming that the presence of Cr prevents the formation of isolated AlFeSi particles in Al-based alloys with Fe concentration. This behavior can be attributed to the lower solubility of Cr in the α -Al matrix when compared to the solubility in the Al–Fe intermetallics.^[48] Similar behavior was observed by Aranda et al.^[6] in Al–Si–Fe alloys with different Cr contents (1%, 3%, and 5%). The presence of Cr decreased the formation of the Al₃FeSi₂ intermetallic compound, and a complex AlSiFeCr intermetallic was observed to occur.

Similar distribution, morphology, and size of the α -Al(Fe,Si)Cr intermetallic phase for the 372 and 374 alloys were observed (Figure 8a,b). According to the partial Al–(3–7)Si– x Cr phase diagrams (Figure 1b,c), the solidification path of the 334 and 374

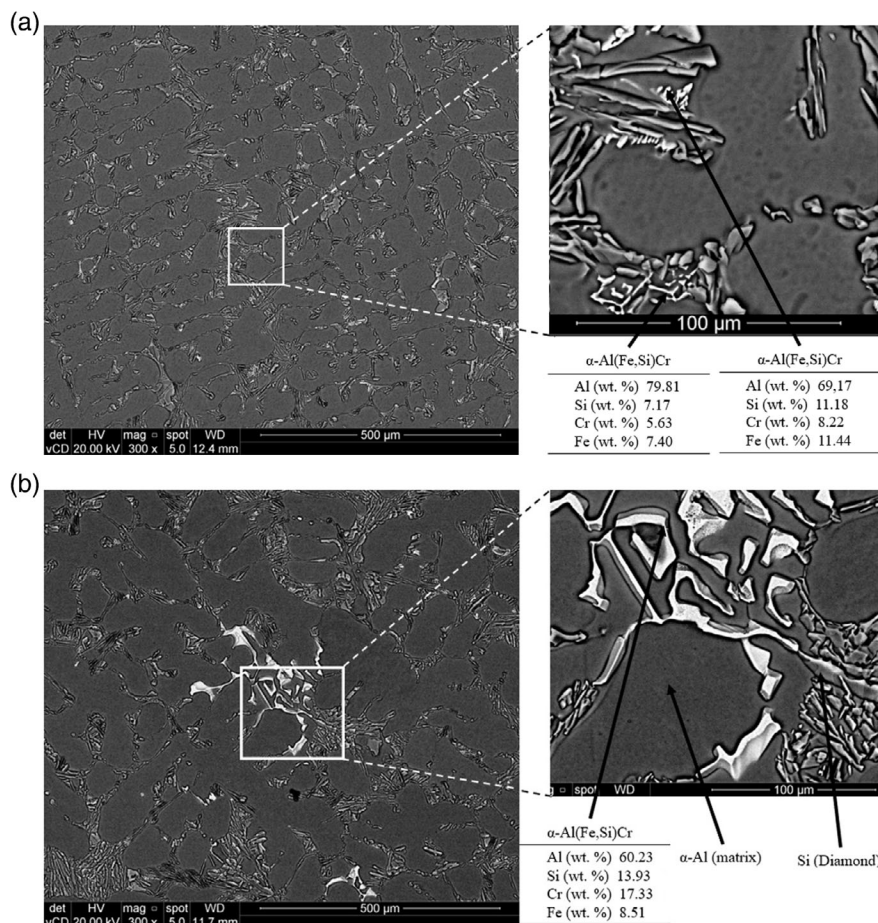


Figure 7. SEM images and EDS analyses of a) 332 and b) 334 alloys.

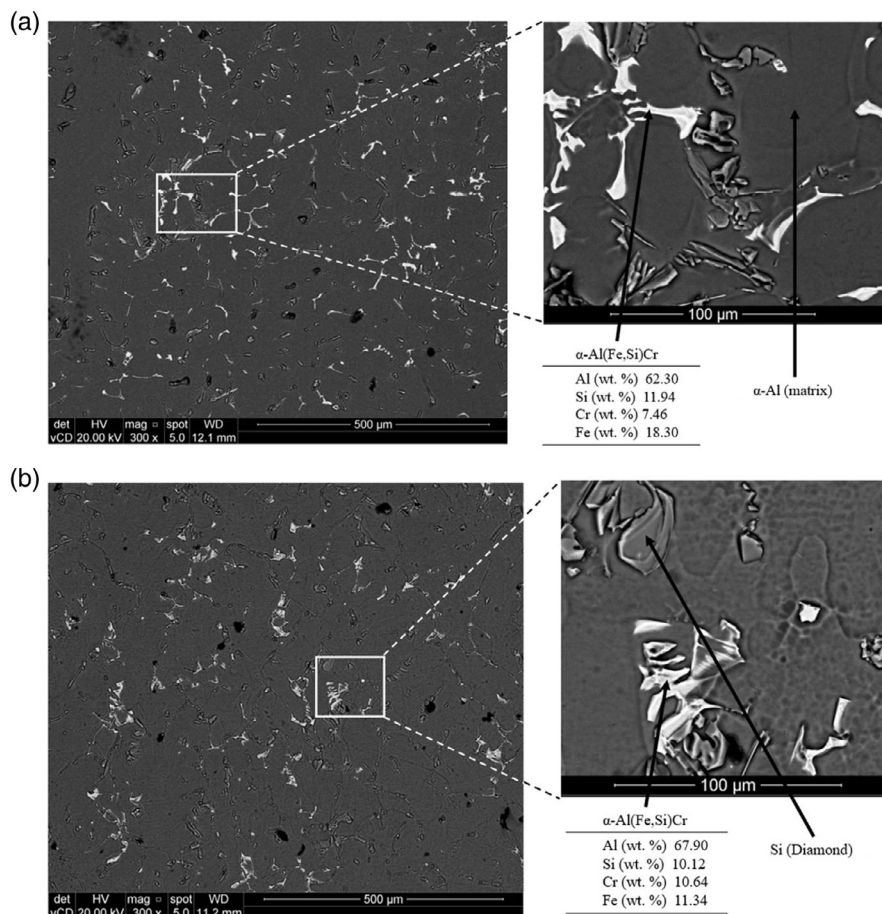


Figure 8. SEM images and EDS analyses of a) 372 and b) 374 alloys.

alloys can be described as $L \rightarrow (L + Al_7Cr) \rightarrow (L^\circ C s^{-1} \alpha-Al + Al_7Cr) \rightarrow (\alpha-Al + Si + Al_7Cr)$, and that of the 332 and 372 alloys as $L \rightarrow (L + \alpha-Al) \rightarrow (L + \alpha-Al + Al_7Cr) \rightarrow (\alpha-Al + Si + Al_7Cr)$.

The main difference between the alloys is related to the primary phase formed during solidification. In the case of the alloys with higher Cr content, the Al_7Cr phase nucleates first, whereas in the alloys with lower Cr content the first phase to be formed is the $\alpha-Al$ matrix. Although the equilibrium phase diagrams indicate the presence of the Al_7Cr phase, this phase was undetected in the investigated alloys. Liu et al.^[48] stated that the formation of AlCr phases may be reduced or suppressed with small Cr addition. In all the alloys, the resulting Si morphology was acicular. According to Hu et al.^[49] the effect of Cr is insignificant on changing the Si morphology of Al–Si-based alloys. According to the results of this work, smaller Cr/Si ratios (372 and 374 alloys) decrease the cooling rates and tip growth rates during solidification, inducing the formation of the eutectic mixture and $\alpha-Al(Fe,Si)Cr$ intermetallics having a coarser and more regular morphology. With the increase in the Cr/Si ratio (332 and 334 alloys) the microstructure morphologies are shown to be more refined and irregular because of the higher solidification rates, which minimize the tendency of solute rejection by the solid phase.

For a better understanding of the solute distribution in the microstructure, **Figure 9** shows EDX mapping images of the Al, Si, Cr, and Fe elements for the alloys with higher Si content. It can be observed that Fe frequently appears together with Cr in the $\alpha-Al(Fe,Si)Cr$ intermetallic phase, irregular Si particles are found in the eutectic mixture regions, and the presence of isolated $\beta-Al_5FeSi$ particles is unobserved.

X-ray diffraction patterns of the alloys are shown in **Figure 10**. The diffractograms show peaks of the $\alpha-Al$ (FCC, matrix) and Si (diamond, isolated particles) and small peaks of the $\alpha-Al(Fe,Cr)Si$ (BCC, Chinese script). For the 372 and 374 higher-Si-containing alloys, it is possible to identify higher $\alpha-Al(Fe,Cr)Si$ and lower Si peaks when compared to the 332 and 334 lower-Si-containing alloys, which permits supposing that the volume fraction of the precipitate increases with increasing alloy Si and Cr contents. The results are in agreement with those reported by Li et al.^[20] and Yang et al.^[21] for Al–Si–Cr alloys with different Cr and Si additions.

3.3. Mechanical Properties

Figure 11a shows the Brinell hardness (HB) variation with the secondary dendrite arm spacing (λ_2) along the length of the alloy

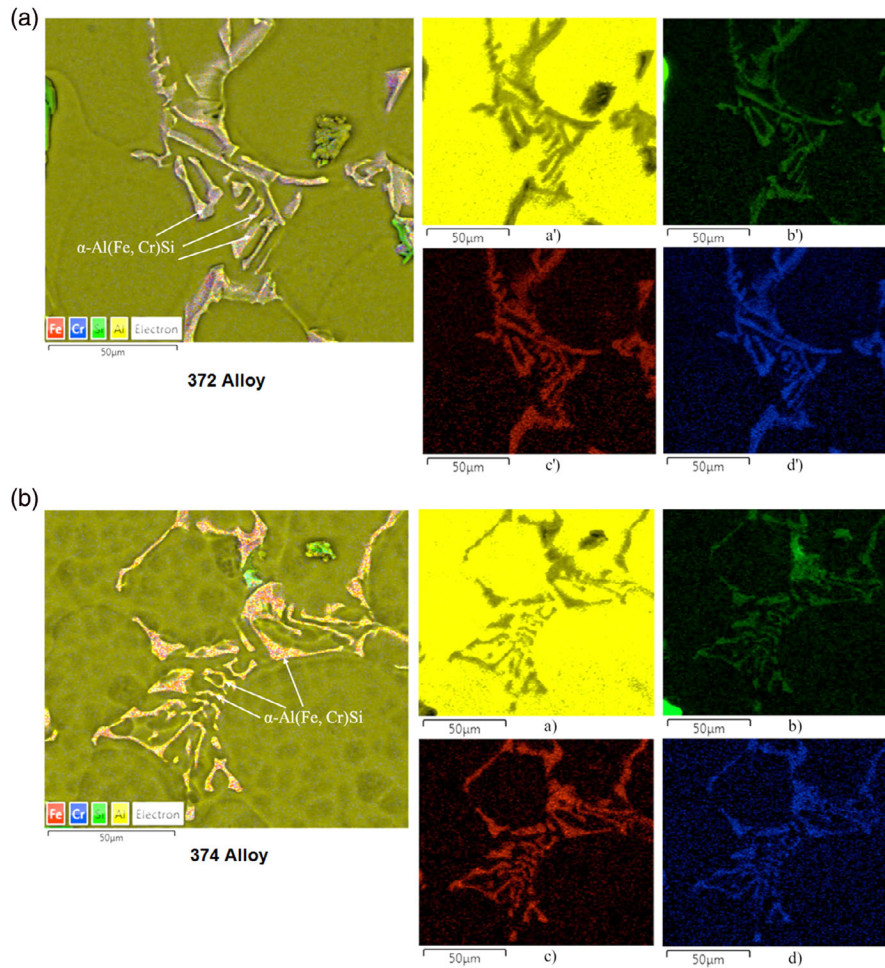


Figure 9. EDX mapping images of the a) 372 and b) 374 alloys showing the distribution of Al, Si, Cr, and Fe elements: a' - a: Al, b' - b: Si, c' - c: Fe, d' - d: Cr.

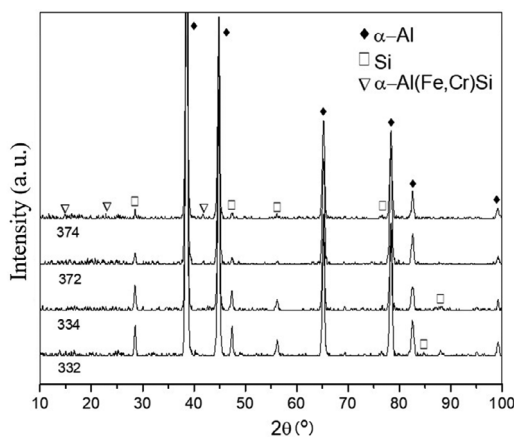


Figure 10. X-ray diffraction patterns of the alloys.

ingots. It is noted that HB shows higher values in the alloys with 3% Si (45–47 HB) when compared to the alloys with 7% Si (40–44 HB). In both cases, a slight variation is observed.

A more sensitive behavior related to the ultimate tensile strength (UTS) was found, as shown in Figure 11b. The tensile strength of the lower-Si-containing alloys achieved values between 112 and 125 MPa with the variation in λ_2 , whereas the alloys with higher Si content showed a noticeable variation between 80 and 120 MPa. It was expected that the alloys with higher Si content would provide better mechanical response because of hard particles.^[50] However, the observed behavior in the investigated alloys could be associated with the formation of α -Al(Fe,Cr)Si particles and their interaction with the α -Al matrix. To verify only the influence of the alloying elements on the solid solution hardness, Vickers tests were conducted in the α -Al matrix in each alloy at TC2, TC5, and TC6 positions (Figure 11c). The results showed that the lower-Si-containing alloys were characterized by very similar values (45–47 HV) independently of the position along the length of the ingots, whereas the alloys having higher Si and Cr contents had the hardness of the matrix increased, mainly at positions farther from the cooled bottom of the ingot. It is believed that this increase is associated with the solute incorporated into the matrix during solidification, which is improved at lower cooling rates.

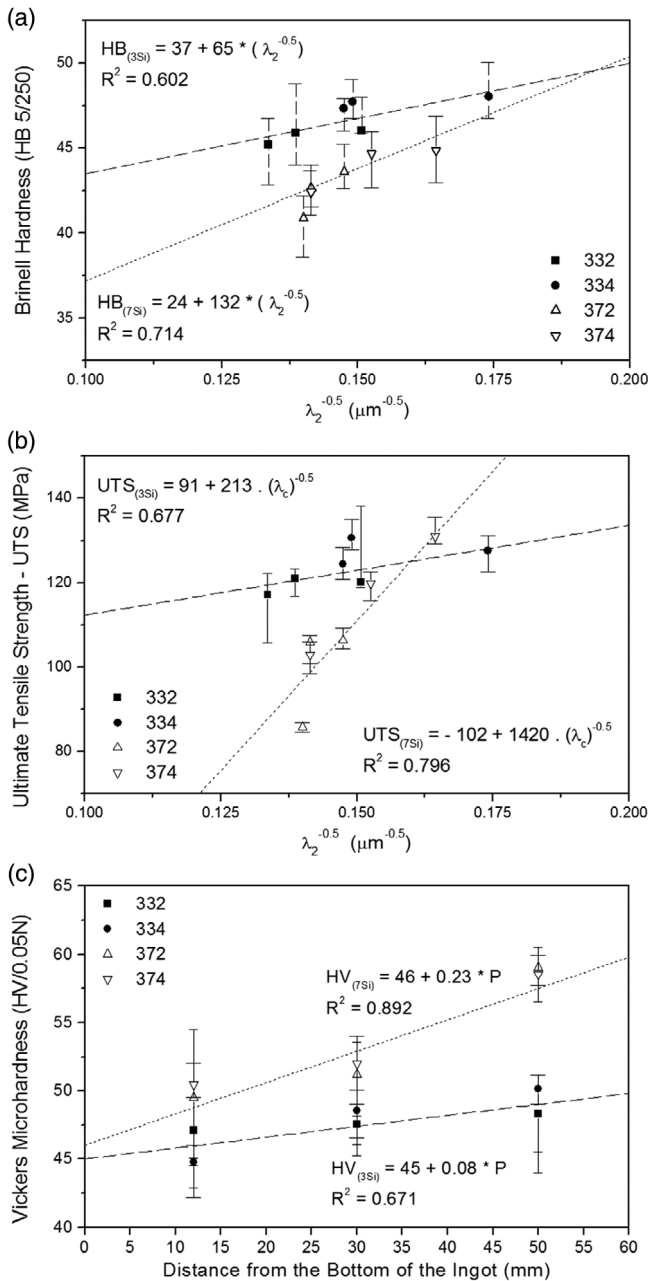


Figure 11. a) Brinell hardness and b) UTS as function of secondary dendrite arm spacing (λ_2). c) Vickers microhardness variation with position along the length of the alloy ingots.

The results of Figure 12a–d are average values of the COF as a function of the sliding distance for all alloys and positions. For the 332 and 372 alloys with lower Cr content, an initial transient friction regime can be observed at the first 50 m sliding distance and after that a steady-state behavior is attained. For the 334 and 374 higher-Cr-containing alloys, the transient stage was noted until the first 25 m sliding distance before achieving the steady-state regime. The initial transient regime occurs due to the surface roughness, which induces the fragmentation and

extraction of material from the surface by abrasion, as suggested by Rao et al.^[51] The 332 and 334 alloys showed similar wear responses in terms of the COF as a function of position as compared to the 372 and 374 alloys. Until 250 m sliding distance, the COF for the positions at 12, 30, and 50 mm of the 332 alloy ingot varied from 0.22 to 0.32 and the 334 alloy from 0.26 to 0.32, while the 372 alloy presented values from 0.23 to 0.35 and the 374 alloy from 0.26 to 0.34. The highest values for the alloys with 7% Si were found at positions near the top of the ingot, and this can be attributed to the higher concentration of particles compared to the other regions.

Vickers tests were performed to verify the hardness of the precipitates, and the average value of the α -Al(Fe,Cr)Si precipitate was found to be ≈ 85 HV and that of the Si particles to be ≈ 100 HV, values higher than that of the α -Al matrix. These hard particles can provide distinguished behavior when uniformly distributed and associated with a hard matrix, helping to protect the material surface against wear. However, if the matrix has lower hardness the particles can plow the material of the matrix.

To better characterize the wear responses, the Archard wear model^[33,34] represented by Equation (1) was used to determine the wear rate (W), given as

$$\frac{V_{\text{disc}}}{S} = k \times \frac{L}{\text{HB}} \quad (1)$$

where k is the wear coefficient, S is the sliding distance, L is the normal applied load, and HB is the disc Brinell hardness. The disc volume loss V_{disc} is calculated as

$$V_{\text{disc}} = \frac{\pi \times D^4}{64r} \quad (2)$$

where r is the pin radius and D is the wear-track diameter. Figure 13a shows that the wear rate increases with the increase in the load–hardness relation or with the decrease in hardness. When comparing the alloys, it can be observed that the smallest wear rate occurs for the alloy with lower Si and higher Cr contents (334 alloy), which is associated with smaller secondary dendritic arm spacings and higher hardness. In contrast, the highest wear rate was noted for the alloy with higher S and lower Cr contents (372 alloys). A curve fit to the points permitted a linear equation to be obtained characterizing the wear rate (W) as a function of the load–hardness relation (L/H) for the alloys, which allowed a wear coefficient $k = 2.88 \times 10^{-3} \text{ mm}^3 \text{ Nm}^{-1}$ to be determined, a value that indicates a mild wear regime. The wear-track surface images obtained by optical microscopy are shown in Figure 13b. The 332 and 334 alloys exhibited more uniform wear-track scars, whereas the 372 and 374 alloys presented irregular wear damages. In all cases, both abrasive and adhesive wear mechanisms were observed. Farhat et al.^[52] proposed a method to express the wear rate (W) related to microstructural features, using the Hall–Petch model to rearrange the Archard law. Figure 13c shows the obtained relations for the analyzed alloys, which permits inserting the equations of $\text{HB} = f(\lambda_2)$ shown in Figure 11a to express the wear rate as a function of the secondary dendrite arm spacing (λ_2).

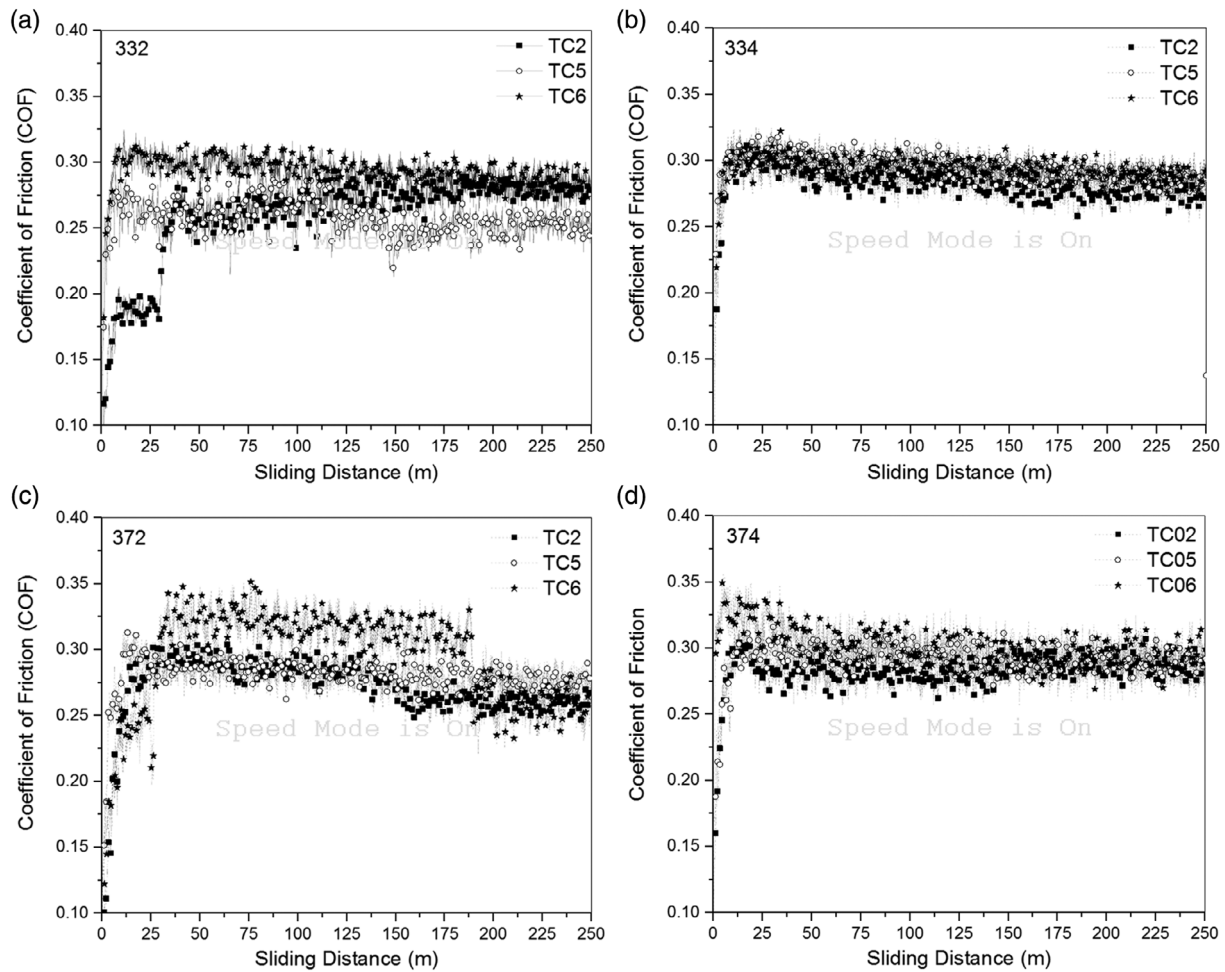


Figure 12. Average values of the COF at different positions for the a) 332, b) 334, c) 372, and d) 374 alloy ingots.

$$W_{(3Si)} = -2.94 \times 10^{-4} + 2.88 \times 10^{-3} \times \left[\frac{L}{37 + 65 \times \lambda_2^{-0.5}} \right] \quad (3)$$

$$W_{(7Si)} = -2.94 \times 10^{-4} + 2.88 \times 10^{-3} \times \left[\frac{L}{24 + 132 \times \lambda_2^{-0.5}} \right] \quad (4)$$

According to the results herein, the wear rate decreases with the decrease in λ_2 , which is in agreement with results of previous works.^[26–53] Such expressions can be used to design solidification conditions with a view to obtaining a particular microstructure feature leading to a desired level of wear behavior.

4. Conclusion

Based on the experimental results obtained in this study, the following main conclusions can be drawn. 1) The Cr

addition to the binary Al–Si alloys promoted the formation of the α -Al(Fe,Si)Cr intermetallic compound, suppressing the precipitation of β -Al₅FeSi intermetallic particles. This confirms that low Cr content has a beneficial effect on minimizing Al–Fe particle formation. 2) The cooling rate and the secondary dendrite arm spacing decreased with the increase in the alloy Si content. The addition of Cr showed an insignificant effect on λ_2 . On the other hand, higher Cr content increased the cooling rate. 3) When the alloys with the same Si concentration are compared, the addition of Cr is shown to improve the mechanical properties, such as hardness and UTS. Empirical experimental equations relating the secondary dendrite arm spacing (λ_2) with mechanical properties were proposed. 4) The COF obtained during the sliding wear analyses was shown to increase slightly for alloys with higher Cr content and coarser microstructures. 5) The wear tests permitted us to obtain correlations relating the wear rate to hardness and λ_2 , with a lower wear rate being associated with lower alloy Si content, higher Cr addition, and smaller λ_2 .

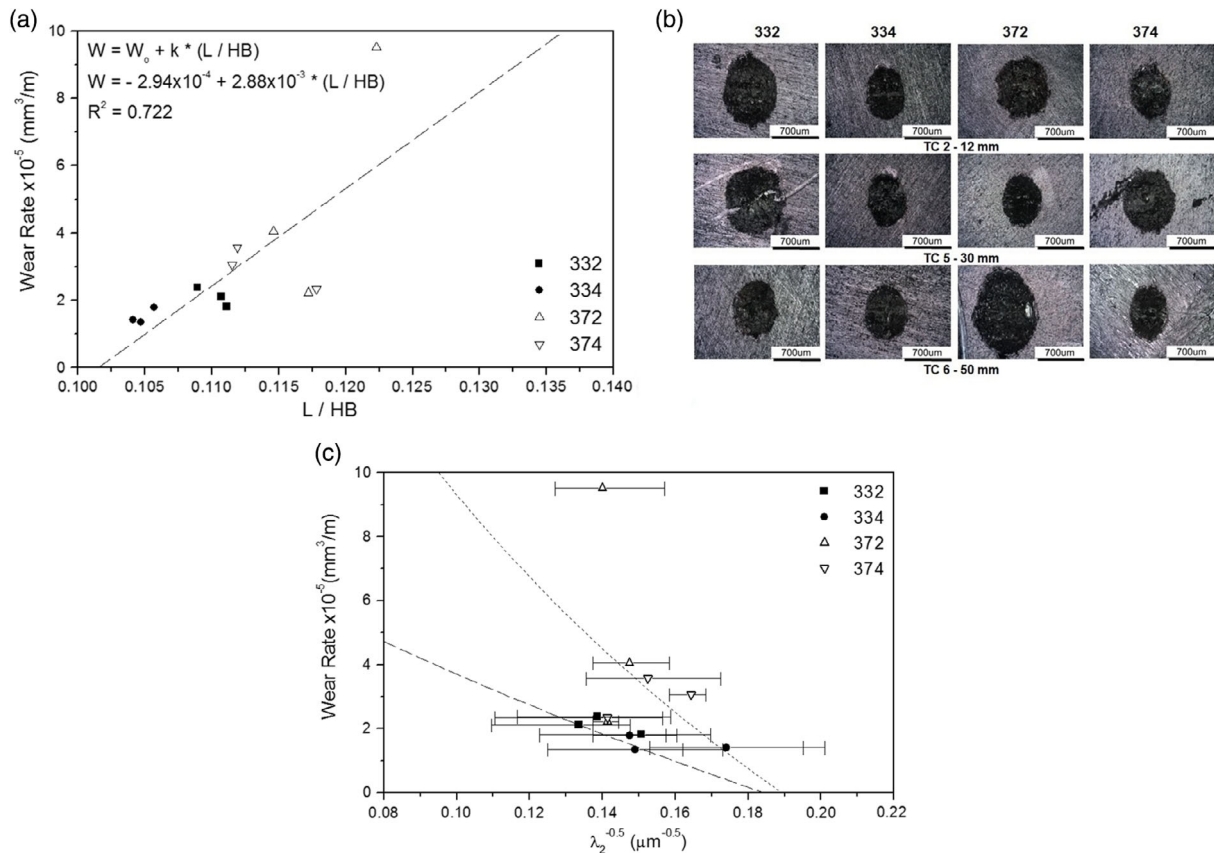


Figure 13. a) Wear rate as a function of hardness, b) wear-track scar images, and c) wear rate as a function of secondary dendrite arm spacing (λ_2).

Acknowledgements

The authors acknowledge the support provided by CNPq (National Council for Scientific and Technological Development: grants: 403303/2016-8 and 301600/2015-5), FINEP (Financiadora de Estudos e Projetos: grant: 0082/16), FAPERGS (Fundação de Amparo à Pesquisa do Rio Grande do Sul), CAPES (Coordenação de Aperfeiçoamento de Pessoal de Nível Superior), and PUCRS (Pontifícia Universidade Católica do Rio Grande do Sul).

Conflict of Interest

The authors declare no conflict of interest.

Data Availability Statement

Research data are not shared.

Keywords

Al-Si-Cr alloys, mechanical properties, microstructures, solidification, wear

Received: December 30, 2020

Revised: February 9, 2021

Published online:

- [1] L. F. Mondolfo, *Aluminum Alloys: Structure And Properties*, Butterworth, London **1976**.
- [2] S. K. Shara, F. Czerwinski, W. Kasprzak, J. Friedman, D. L. Chen, *Mater. Sci. Eng. A* **2016**, 652, 353.
- [3] M. Tocci, R. Donnini, G. Angella, A. Pola, *Mater. Character.* **2017**, 123, 75.
- [4] G. Li, H. Liao, X. Suo, Y. Tang, U. S. Dixit, P. Petrov, *Mater. Sci. Eng. A* **2018**, 790, 90.
- [5] M. S. Kaiser, S. H. Sabbir, M. S. Kabir, M. R. Soummo, M. Al Nurb, *Mater. Res.* **2018**, 21–4, 1.
- [6] V. A. Aranda, I. A. Figueroa, G. González, J. A. García-Hinolosa, G. A. Lara-Rodríguez, *Metals* **2019**, 9–136, 3.
- [7] G. Gustafsson, T. Thorvaldsson, G. L. Dunlop, *Metall. Mater. Trans. A* **1986**, 17, 45.
- [8] L. Backerud, G. Chai, J. Tamminen, *Solidification Characteristics Of Aluminum Alloys. Vol. 2 – Foundry Alloys*, American Foundrymans Society/Skanaluminium, Oslo **1990**, pp. 71–84.
- [9] S. P. Gupta, *Charact.* **2009**, 49–4, 269.
- [10] N. A. Belov, A. A. Aksenov, D. G. Eskim, *Impurity And Alloying Elements*, Taylor and Francis, New York **2002**.
- [11] C. M. Dinnis, J. A. Taylor, A. K. Dahle, *Scr. Mater.* **2005**, 53, 955.
- [12] G. Sha, K. A. Q. O'Reilly, B. Cantor, J. Worth, R. Hamerton, *Mater. Sci. Eng. A* **2001**, 304–306, 612.
- [13] S. Seiffedine, S. Johansson, I. I. Svensson, *Mater. Sci. Eng. A* **2008**, 490, 385.
- [14] A. Verma, S. Kumar, P. S. Grant, K. A. Q. O'Reilly, *J. Alloys Compd.* **2012**, 555, 274.
- [15] S. G. Shabestari, M. Mahmudi, M. Emami, J. Campbel, *Int. Cast Metals Res.* **2002**, 15, 17.

- [16] S.G. Shabestari, *Mat. Sci. Eng. A* **2004**, 383, 289.
- [17] X. Cao, J. Campbel, *Metall. Mater. Trans. A* **2004**, 35, 1425.
- [18] C. Bidmeshki, V. Abouei, H. Saghafian, S. G. Shabestari, M. T. Noghani, *J. Mater. Res. Technol.* **2016**, 5–3, 250.
- [19] M. Mahta, M. Emamy, A. Daman, A. Keyvani, J. Campbell, *Int. Cast Metals Res.* **2005**, 18–2, 73.
- [20] Y. Li, Y. Yang, Y. Wu, Z. Wei, X. Liu, *Mater. Sci. Eng. A* **2011**, 528, 4427.
- [21] Y. Yang, S-Y. Zhong, Z. Chen, M. Wang, N. Ma, H. Wang, *J. Alloys Compd.* **2015**, 647, 63.
- [22] B. Grushko, D. Pavlyuchkov, *J. Alloys Compd.* **2015**, 622, 327.
- [23] S. Cui, *J. Alloys Compd.* **2017**, 698, 1038.
- [24] O. B. Ifeanyi, N. E. Nkem, A. F. Amaechi, *J. Sci. Eng. Res.* **2016**, 3 383.
- [25] R. Ahmad, *Int. J. Mater. Sci. Res.* **2018**, 1 32.
- [26] C. T. Ache, M. M. Lopes, B. P. Reis, A. Garcia, C. A. Santos, *Adv. Eng. Mater.* **2020**, 1901145, 1.
- [27] T. M. Ribeiro, E. Catellan, A. Garcia, C. A. Santos, *J. Mater. Res. Technol.* **2020**, 9–3, 6620.
- [28] American Society for Testing and Materials, *Standard Guide For Preparation Of Metallographic Specimens*, ASTM E 3ASTM International, West Conshohocken, PA **2017**.
- [29] American Society for Testing and Materials, *Standard Practice For Microetching Metals And Alloys*, ASTM E 407ASTM International, West Conshohocken, PA **2015**.
- [30] American Society for Testing and Materials, *Standard Test Methods For Brinell Hardness Of Metallic Materials*, ASTM E 10a, ASTM International, West Conshohocken, PA **2017**.
- [31] American Society for Testing and Materials, *Standard Test Methods For Tension Test Of Metallic Materials*, ASTM E 8ASTM International, West Conshohocken, PA, **2016**.
- [32] American Society for Testing and Materials. *Standard Test Methods For Vickers Hardness And Knoop Hardness Of Metallic Materials* ASTM E 92, ASTM International West Conshohocken, PA, **2017**.
- [33] J. F. Archard, *J. Appl. Phys.* **1953**, 24, 981.
- [34] J. K. Lancaster, *Wear* **1990**, 141, 159.
- [35] E. M. Costa, C. E. Costa, F. D. Vecchia, C. Ricka, M. Scherer, C. A. Santos, B. A. Dedavid, *J. Alloys Compd.* **2009**, 448–1, 89.
- [36] S. Farahany, A. Ourdjini, M. H. Idris, S. G. Shabestari, *J. Therm. Anal. Calor.* **2013**, 114–2, 705.
- [37] S. M. Igajini, K. Venkateswarlu, S. A. Kori, *Int. J. Eng. Sci. Tech.* **2012**, 3–6, 257.
- [38] M. D. Peres, C. A. Siqueira, A. Garcia, *J. Alloys Compd.* **2004**, 381, 168.
- [39] P. R. Goulart, J. E. Spinelli, W. R. Osorio, A. Garcia, *Mater. Sci. Eng. A* **2006**, 421, 245.
- [40] O. Engler, S. Miller-Jupp, *J. Alloys Compd.* **2016**, 689, 998.
- [41] Y. Han, K. Ma, C. Wang, H. Nagaumi, *Precipitation Behavior of Dispersoids in Al-Mg-Si-Cu-Mn-Cr Alloy During Homogenization Annealing*, ICAA13 Springer, Pittsburgh **2012**, pp. 1817–1824.
- [42] A. Kumar, G. Sharma, C. Sasikumar, S. Shamim, H. Singh, *Appl. Mech. Mater.* **2015**, 789–790, 95.
- [43] T. A. Costa, M. Dias, L. G. Gomes, O. L. Rocha, A. Garcia, *J. Alloys Compd.* **2016**, 683, 485.
- [44] T. A. Costa, A. L. Moreira, D. J. Moutinho, M. Dias, I. L. Ferreira, J. E. Spinelli, O. L. Rocha, A. Garcia, *Mater. Sci. Technol.* **2015**, 31 1103.
- [45] B. Zang, M. Garro, C. Tagliano, *Metall. Sci. Technol.* **2003**, 21, 3.
- [46] M. B. Djurdjevic, M. A. Grzincic, *Ach. Foundry Eng.* **2012**, 12, 19.
- [47] H. Zhan, B. Hu, *Mater. Charact.* **2018**, 142, 602.
- [48] B. Liu, *J. Minerals Metals Mater. Soc.* **2012**, 64–2, 316.
- [49] P. Hu, Y. Su, W. P. Chen, Y. Jiang, *Adv. Mater. Res.* **2013**, 652, 1023.
- [50] R. Saravanan, R. Sellamuthu, *Proc. Eng.* **2014**, 97, 1348.
- [51] R. N. Rao, S. Das, D. P. Mondal, G. Xixit, *Wear* **2009**, 267, 1688.
- [52] Z. N. Farhat, Y. Ding, D. O. Northwood, A. T. Alpas, *Mater. Sci. Eng. A* **1996**, 206, 302.
- [53] B. P. Reis, M. M. Lopes, A. Garcia, C. A. Santos, *J. Alloys Compd.* **2018**, 764, 267.